PHYSICAL REVIEW B **98**, 115427 (2018)

Interface excitons at lateral heterojunctions in monolayer semiconductors

Ka Wai Lau,[1] Calvin,[1] Zhirui Gong,[2,1,*] Hongyi Yu,[1] and Wang Yao[1]
[1]*Department of Physics, and Center for Theoretical and Computational Physics, The University of Hong Kong, China*
[2]*College of Physics and Energy, Shenzhen University, Shenzhen 518060, People's Republic of China*

(Received 25 July 2018; published 17 September 2018)

We study the interface exciton at lateral type II heterojunctions of monolayer transition metal dichalcogenides (TMDs), where the electron and hole prefer to stay at complementary sides of the junction. We find that the 1D interface exciton has giant binding energy in the same order as 2D excitons in pristine monolayer TMDs although the effective radius (electron-hole separation) of interface exciton is much larger than that of 2D excitons. The binding energy, exciton radius, and optical dipole strongly depends on the band offset at the junction. The intervalley coupling induced by the electron-hole Coulomb exchange interaction and the quantum confinement effect at interfaces of a closed triangular shape are also investigated. Small triangles realize 0D quantum dot confinement of excitons, and we find a transition from nondegenerate ground state to degenerate ones when the size of the triangle varies. Our findings may facilitate the implementation of the optoelectronic devices based on the lateral heterojunction structures in monolayer semiconductors.

DOI: 10.1103/PhysRevB.98.115427

I. INTRODUCTION

Heterostructures between conventional three-dimensional (3D) semiconductors has inspired the inventions of the modern electronic devices such as high speed transistors [1], diode lasers [2], light-emitting diodes [3], and solar cells [4]. Thanks to the development of nanotechnology, we are able to engineer heterostructures on the nanoscale for high-speed optoelectronic devices. In III-V and II-VI semiconductors, various nanoscale heterostructures such as quantum wells, superlattices, and core-shell nanodots and nanowire have been widely studied [5–7]. Emerged as a new class of semiconductors in the two-dimensional (2D) limit [8–12], monolayers of group-VIB transition metal dichalcogenides (TMDs) possess a visible range direct gap, exotic properties associated with valley degeneracy, and new geometries for realizing various heterostructures, which provide new platforms to study the physics and applications at semiconductor heterostructures [13–16]. By stacking different TMDs monolayers which are then bound together by the weak interlayer Van der Waals forces, vertical heterostructures have been realized recently, e.g., $\mathrm{MoX_2/WX_2}$ (X=Se, S) heterobilayers [17–24], which can be analogs of the III-V semiconductor double heterojunctions.

Besides the vertical heterostructures, two-dimensional materials also make possible heterostructures of a unique planar geometry. Two different TMDs seamlessly connected in a single monolayer has been realized experimentally already [25–36]. A more recent development is on the growth of various lateral heterostructures, multiheterostructures and superlattices for TMDs [37]. The possibility to form an atomically sharp and straight lateral interface of different compounds [33,37] points to exciting opportunities towards device applications based on the lateral heterojunctions, as well as a new geometry to realize quantum wires and even quantum dots in the monolayer semiconductors. The lateral heterojunctions can also be realized in an alternative way, by electrostatic gating to define lateral p-n junctions [38–40]. The recent development shows that the width of the electric gate in the monolayer $\mathrm{MoS_2}$ can be narrowed down to 1 nm by using a single-walled carbon nanotube as the gate electrode [41].

In most of the vertical and lateral heterostructures formed between different TMDs monolayers, they feature a type-II band alignment, where the conduction and valence band edge locate in different TMDs. The strong Coulomb interaction binds electron and hole to form an exciton at the interface. In contrast to a 2D exciton formed in pristine monolayer TMD, the electron and hole at the interface will be spatially separated because of the type-II band alignment, and such an interface exciton can have lower energy, being an excitonic ground state in the heterostructures. The properties of such interface excitons can be essential to determine the optical response of the lateral heterostructures of TMDs. In vertical heterojunctions $\mathrm{MoX_2/WX_2}$ heterobilayers, such an interface exciton has already been investigated theoretically and experimentally [23,24,42–46]. Due to the spatial separation of electron and hole, interlayer excitons in $\mathrm{MoX_2/WX_2}$ heterobilayers have shown long lifetime exceeding nanoseconds [23,24] and electrostatically tunable resonance [47] which are highly desirable for the realization of excitonic circuits and condensation [48,49]. Interestingly, the inevitable twisting and lattice mismatch in the heterobilayers can give rise to novel light coupling properties [42–46]. Albeit the novel and appealing properties discovered, the interface excitons in the heterobilayers of 2D semiconductors are analogues of those in the conventional heterostructures bulk semiconductors, for example the spatially indirect excitons in a III-V double quantum well. The realization of lateral heterostructures in monolayer TMDs opens up new opportunities to extend the

---

[*] gongzr@szu.edu

study of interface exciton from two-dimensional interface to the one-dimensional (1D) interface. The 1D interface exciton mode may shed light on novel optoelectronic devices based on these atomically thin 2D lateral heterostructures. Moreover, such 1D interface excitons may also become relevant in lateral p-n junctions in monolayers TMDs [38–40].

Here, we theoretically study the interface excitonic states at lateral heterojunctions of the monolayer TMDs. The physical properties of a one-dimensional type-II interface exciton such as the binding energy, exciton radius (i.e., electron-hole separation), longitudinal-transverse splitting by the electron-hole exchange, and optical dipole are investigated as a function of band offset at the interface. We adopted two different approaches to calculate the interface exciton states. One approach bases on a real-space tight-binding (TB) model, and the other approach uses the perturbation expansion in a hydrogenlike basis in effective mass approximation. We show that with the increase of the band offset at the interface, the exciton radius increases as well and can become several times larger than that of the 2D excitons in homogeneous monolayer TMDs. In the meantime, the decrease in the exciton binding energy is not as significant, remaining in the same order as the 2D exciton, because of the weaker screening of Coulomb interaction as electron-hole separation increases. Due to spatial indirect nature of interface exciton, the optical transition dipole decreases fast with the increase of band offset, which, at a typical band offset of 300 meV, is about one order of magnitude smaller than that of 2D exciton. We also investigated lateral heterostructures with a closed triangular-shaped interface which effectively realize a 0D quantum dot confinement of exciton. Such a quantum dot uniquely features the quantum confinement of one carrier by the band offset of the interfaces and binding of the other carrier in the proximity exterior by the strong Coulomb. We find two distinct scenarios of energy level schemes and valley optical selection rules of the interface exciton at small and large quantum dot size, respectively, which can be exploited for optical quantum controls.

The paper is organized as follows. In Sec. II, we introduce the Hamiltonian of the exciton of lateral structures in the effective mass approximation. We study the interface exciton at the 1D p-n and p-n-p heterojunctions of monolayer semiconductors in Sec. III. The numerical results of the physical observables of interface exciton are also shown in Sec. III. In Sec. IV, we show the numerical calculations of the interface exciton at the 0D quantum dot type triangular lateral heterostructure. We conclude in Sec. V.

II. HAMILTONIAN IN THE EFFECTIVE MASS APPROXIMATION

It is shown that electronic properties of monolayer TMDs near the Fermi surface are effectively described by the three-band model involving all d orbitals of the transition metal atom [8]. In the low energy excitation limit where only the electron in the vicinity of the valance band edge is excited by light field to the vicinity of the conduction band edge, both the electron in the conduction band and the hole left in the valence band can be approximately described by the effective mass model. In this sense, the periodic parts of the electron and hole Bloch wave functions are omitted and only the profiles of the electron and hole Bloch wave functions are taken into consideration in the following discussion. Together with the attractive Coulomb interaction and the lattice potentials, the type II interface exciton at the interface can be described by the following Hamiltonian

$$H = -\frac{\hbar^2}{2m_e}\nabla^2_{\mathbf{r}_e} - \frac{\hbar^2}{2m_h}\nabla^2_{\mathbf{r}_\mathrm{h}} + V_\mathrm{C}(|\mathbf{r}_e - \mathbf{r}_h|) + V_\mathrm{e}(\mathbf{r}_e) + V_\mathrm{h}(\mathbf{r}_h), \tag{1}$$

where m_e (m_h) is the electron (hole) effective mass, and $\mathbf{r}_e$ ($\mathbf{r}_h$) denotes the position coordinates of the electron (hole). The lattice potentials of electron and hole $V_\mathrm{e}(\mathbf{r}_e)$ and $V_\mathrm{h}(\mathbf{r}_h)$ depend on the different geometries of the lateral heterostructures.

Here, the Coulomb interaction $V_\mathrm{C}(|\mathbf{r}_e - \mathbf{r}_h|)$ between the electron and hole in the 2D limit reads [50,51]

$$V_\mathrm{C}(r) = -\frac{e^2\pi}{2r_0}\left(H_0\left(\frac{r}{r_0}\right) - Y_0\left(\frac{r}{r_0}\right)\right), \tag{2}$$

where H_n and Y_n denote Struve function and Bessel function of the second kind, respectively. The former researches demonstrated that in monolayer TMDs the quasi-2D geometry leads to a distance-dependent effective dielectric screening [52–55]. For monolayer TMDs, the parameter r_0 is on the order of a few nm, which is comparable to the Bohr radius of a free 2D exciton [52,53].

III. INTERFACE EXCITON AT 1D P-N AND P-N-P HETEROJUNCTIONS

A. Type II interface in monolayer TMDs

A lateral type-II interface in monolayer TMDs can be implemented in two setups. The first is a lateral heterojunction seamlessly formed between different TMDs [29–32] as shown in Figs. 1(a) and 1(d). In such cases, the type-II interface is atomically sharp. The conduction and valence band edges as functions of position are regarded as the step functions. The other setup shown in Figs. 1(b) and 1(e) is lateral p-n or p-n-p junctions electrostatically created in a monolayer TMD by separate back gates, which has been studied experimentally [38–40]. Such a setup realizes a gentle type-II interface with a finite width of the interfaces w. It should be indicated that although the band offset V_0 and the width of the interfaces w cannot be tuned for the former lateral heterojunction which are formed by different TMDs, they can be tuned for the latter lateral heterojunction because the type II band alignment results from the tunable electrostatic gating.

We are interested in the binding energy and wave function of the interface exciton ground state, which determines the stability and optoelectronics properties of the interface exciton. By the interface potentials, electron and hole prefer to stay at complementary sides of the interface, while the Coulomb interaction $V_\mathrm{C}(|\mathbf{r}_e - \mathbf{r}_h|)$ attempts to bind the electron and hole. The properties of the interface exciton therefore depends on the competition between the band offset and the Coulomb interaction, which are then tunable by the width w of the interface and the magnitude of the conduction and valence band edge offsets V_0. The effective dielectric

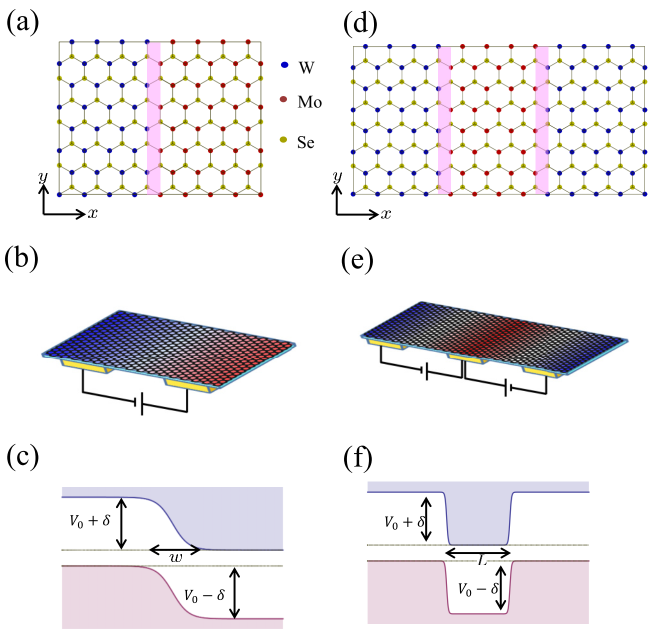

FIG. 1. (a),(d) Schematics of the single and double heterojunctions formed by $MoSe_2$ and WSe_2. The blue, red, and yellow spheres, respectively, denote W, Mo, and Se atoms. The purple shadow regions denote the type II interfaces. (b),(e) Schematics of the monolayer TMDs p-n junction defined by the electrostatic gating. The red and blue regions denote the n and p regions, respectively. (c),(f) Illustration of the band edge profile across the single lateral junction in (a) or (b) and the double lateral junctions in (d) or (e). Here, w is the width of the interface, which is zero for the case of (a) and (d), and has a finite value for the gate defined junctions in (b) and (e). V_0 is the average lattice potential of electron and hole in (a) or (d) and gate voltage in (b) or (e). The δ characterizes the difference of the band offsets for electron and hole.

screening of Coulomb interaction varies with distance, and for large distance between electron and hole the screening effect is substantially reduced. As we will show, this is important for the interface exciton to have strong binding energy, even though the spatial separation between the electron and hole is much larger than the Bohr radius of the 2D exciton.

B. Solving the eigenproblem using Born-Oppenheimer approximation

Since $V_{\mathrm{I}}(\mathbf{r}_e,\mathbf{r}_h)=V_{\mathrm{e}}(\mathbf{r}_e)+V_{\mathrm{h}}(\mathbf{r}_h)$ possesses translational symmetry while Coulomb interaction possesses rotational symmetry, incompatible symmetries make it impossible to obtain analytical solutions for the Schrödinger equation governed by the Hamiltonian in Eq. (1). We rewrite the above Hamiltonian with the center-of-mass motion and relative motion of the electron-hole pair as

$$H=-\frac{\hbar^2}{2M}\nabla_{\mathbf{R}}^2-\frac{\hbar^2}{2\mu}\nabla_{\mathbf{r}}^2+V_{\mathrm{C}}(r)+V_{\mathrm{I}}(\mathbf{R},\mathbf{r}),\tag{3}$$

where the center-of-mass and relative space coordinates are

$$\begin{cases}\mathbf{R}=\frac{1}{M}(m_e\mathbf{r}_e+m_h\mathbf{r}_h)\\ \mathbf{r}=\mathbf{r}_e-\mathbf{r}_h\end{cases}\tag{4}$$

with total mass $M=m_e+m_h$ and reduced mass $\mu=m_em_h/(m_e+m_h)$. Due to the 2D nature of TMDs, these coordinates only have two components which means $\mathbf{R}=(X,Y)$ and $\mathbf{r}=(x,y)$. Obviously, the total mass is at least four times greater than the reduced mass ($M\geqslant4\mu$), which implies that the center-of-mass motion is a relatively slow one in comparison with the relative motion. Under this circumstance, we can apply the Born-Oppenheimer approximation (BOA) here and in zeroth order BOA the eigenwavefunction is a product state as

$$\Phi(\mathbf{R},\mathbf{r})=\Psi(\mathbf{R})\Theta(\mathbf{R},\mathbf{r}).\tag{5}$$

For lateral heterojunctions $V_{\mathrm{I}}(\mathbf{r}_e,\mathbf{r}_h)$ possesses translational symmetry along the y direction as shown in Figs. 1(a) and 1(d). The interface potential is numerically modelled with $V_{\mathrm{e}}(x_e)=\frac{V_0+\delta}{2}(1-\tanh(\frac{x_e}{w}))$ and $V_{\mathrm{h}}(x_h)=-\frac{V_0-\delta}{2}(1-\tanh(\frac{x_h}{w}))$, where w is the width of the interface which characterizing the sharpness of the band offset. As $V_{\mathrm{I}}(\mathbf{R},\mathbf{r})$ is independent of Y, the envelope function remains to be a plane wave in the Y direction, so we rewrite the center-of-mass motion part as $\Psi(\mathbf{R})=\Psi(X)e^{iP_YY}$. Since P_Y stands for the y-component wave vector corresponding to a kinetic energy $\hbar^2P_Y^2/2M$, obviously $P_Y=0$ for the ground state of type-II interface exciton. Then the corresponding Schrödinger's equations for the relative motion and center-of-mass motion read

$$\left[-\frac{\hbar^2}{2\mu}\nabla_{\mathbf{r}}^2+V_{\mathrm{C}}(r)+V_{\mathrm{I}}(X,\mathbf{r})\right]\Theta(X,\mathbf{r})=E(X)\Theta(X,\mathbf{r}),\tag{6}$$

$$\left[-\frac{\hbar^2}{2M}\frac{\partial^2}{\partial X^2}+E(X)\right]\Psi(X)=E_g\Psi(X).\tag{7}$$

The energy $E(X)$ plays the role of an effective potential in Eq. (7), which leads to the ground state $\Psi(X)\Theta(X,\mathbf{r})$ of type-II interface exciton with corresponding ground state energy E_g. To numerically solve Eq. (6), we adopted two different approaches: One is the solution based on a real-space tight-binding model for the relative part Hamiltonian $H_r=-\frac{\hbar^2}{2\mu}\nabla_{\mathbf{r}}^2+V_{\mathrm{C}}(r)+V_{\mathrm{I}}(X,\mathbf{r})$, and the other is a perturbative expansion of H_r with a hydrogenlike basis of the effective mass model. Details of both approaches can be found in the numerical results section below.

C. Physical observables and the electron-hole overlap

Before we present the numerical results we would like to introduce several important physical observables first. When applying BOA and obtaining the eigenwavefunction of type-II interface excitons, we can straightforwardly calculate the binding energy, effective radius, optical dipole, and the intervalley coupling of the interface excitons [56].

The binding energy of type-II interface exciton is defined as $E_b=E_f-E_g$, where E_f is the energy of a noninteracting electron-hole pair at the interface. The effective radius is straightforwardly calculated as

$$a_b=\sqrt{\iint d\mathbf{r}dX\mathbf{r}^2|\Psi(X)\Theta(X,\mathbf{r})|^2},\tag{8}$$

which measures the spatial separation between the electron and hole.

Another important observable is the optical dipole of the interface exciton defined as

$$D(V_0) = \langle c|\mathbf{A}\cdot\mathbf{P}|v\rangle \int dX\Psi(X)\Theta(X,0), \tag{9}$$

which relates to the lifetime of type-II interface exciton in TMDs. Here, $|c\rangle(|v\rangle)$ is the periodic part of the Bloch function in the conduction (valance) band, $\mathbf{A}$ is the vector potential of the light field, and $\mathbf{P}$ is the momentum operator. If we refer D_0 as the value of $D(V_0)$ at $V_0 = 0$ (i.e., that of the 2D exciton in the absence of interface [57]), $|D(V_0)/D_0|$ is then the dimensionless ratio between the dipole of interface exciton and the 2D exciton. In contrast with the optical dipole of 2D excitons, there is an additional integral over the X direction whose value depends on the wave-function profile along the X direction. Additionally, $\mathbf{r} = 0$ in the relative part of the wave function $\Theta(X,\mathbf{0})$ indicates that the recombination of the electron and the hole in the exciton occurs only when they exactly locate at the same position. In this sense, the electron and hole will become harder to recombine with each other and thus results in a longer lifetime due to the decreased optical dipole. As we will show that below the amount of overlap between the electron and hole can be controlled by $V_\mathrm{I}(\mathbf{R},\mathbf{r})$.

As we can see, the electron-hole overlap plays an important role in Eq. (8) and Eq. (9). For a ground state of the 2D exciton, it closely resembles s orbitals, so a relatively large optical dipole $D(V_0 = 0)$ is expected. However for large V_0 the wave-function overlap between the electron and hole is greatly reduced.

Besides the separation of the electron-hole pair and optical dipole $D(V_0)$, the electron-hole overlap also affects other properties of the type-II interface exciton such as intervalley coupling induced by Coulomb exchange interaction [56]. It was proved that under broken threefold rotation symmetry in monolayer TMDs, the excitonic spectrum could have a finite valley exchange interaction even in the ground state which is induced by exchange Coulomb interaction between electrons and holes [56]. In the presence of $V_\mathrm{I}(\mathbf{R},\mathbf{r})$, translational symmetry is only preserved in the y direction, breaking the threefold rotation symmetry. Thus lateral heterojunctions not only decrease the electron-hole overlap, but also results in a nonvanishing valley-exchange term J. Such a term opens a coupling channel between $+K$ and $-K$ valleys which is normally suppressed in monolayer TMDs due to large momentum difference. In a quasi-1D system, the intervalley coupling strength is written as

$$J = \left(\frac{at}{E_g}\right)^2 \sum_{P_X} V_\mathrm{C}(P_X, P_Y = 0) P_X^2 |\psi(P_X)|^2, \tag{10}$$

where a is the lattice constant, t is the hopping constant, and $V_\mathrm{C}(P_X, P_Y)$ is Coulomb interaction in the momentum space. Here, $\psi(P_X) = \frac{1}{\sqrt{L_X}} \sum_X \Phi(X, \mathbf{r} = 0) exp(iP_X X)$ is the electron-hole overlap in the $X-$ component momentum space. Since the electron-hole overlap is controlled by the strength of the band offset, a tunable intervalley coupling is expected in the lateral heterojunction of TMDs.

It is important to note that the above described zeroth-order BOA is valid only in the adiabatic limit where the gradient of the band offset caused transition probability is much smaller than the energy level spacing between the ground state and any excited state in Eq. (6). Detailed justification shall be referred to the appendix or literature about generalized BOA [58,59]. For the current eigenproblem of type-II interface exciton in TMDs, we will numerically justify that the zeroth order BOA is sufficient.

We will take $\mathrm{MoSe_2/WSe_2}$ heterojunctions as our example in subsequent sections of type-II interface excitons. It is trivial to generalize our method to other sharp TMDs lateral interfaces.

D. Numerical results based on TB model

In order to obtain the TB model, we discretize Eq. (6) in the real space. We take a unit in the x direction as a and the y direction as $\frac{\sqrt{3}}{2}a$, where $a = 3.325$ Å is the lattice constant. The lattice constant of $\mathrm{WSe_2}$ and $\mathrm{MoSe_2}$ closely matches so it is legitimate to assume the same lattice constant across the heterojunctions [20,60]. A 72×84 supercell and the open boundary conditions for both directions are taken into consideration. We consider an armchair interface in the following calculation, while it will give almost the identical results when changing the armchair edge to any other type of the interface. Previous studies [60,61] show that the conduction and valence bands are accurately described by d orbitals of the metal atoms, while the orbitals of the chalcogenides play a minor role. Hence we only consider the metal atoms in our TB model, and the nearest-neighbor hopping is $t = -\hbar^2/3a^2\mu$ between metal atoms. One of the advantages of applying the TB model is that $V_\mathrm{C}(r)$ and $V_\mathrm{I}(\mathbf{R},\mathbf{r})$ are exactly diagonalized. It is noticed that the on-site electrostatic energies $U = V_C(r = 0)$ are divergent. Since for a type II alignment the electron and hole barely can occupy the same site, a large value of the on-site electrostatic energies U is assumed in our calculation in order to make the calculation convergent.

The effective masses of the electron and hole are chosen as $m_e = m_h = 0.32m_0$ and thus the reduced mass is $\mu = 0.16m_0$ with free electron mass m_0. The width of the interface is chosen as $w = 0.1a$ to model a very sharp band offset in order to simulate the single or double heterojunctions. Here, r_0 in the effective Coulomb interaction is chosen as $r_0 = 75$ Å [53]. A symmetric heterojunction ($\delta = 0$) is considered unless otherwise specified.

By solving Eq. (7), the binding energy E_b, effective radius a_b, and optical dipole ratio $|D(V_0)/D_0|$ versus different strength of the band offset V_0 are shown in Fig. 2. We also depict those physical observables when different on-site electrostatic energies U are chosen. The red sphere, blue triangle, and magenta diamond symbols, respectively, represent $U = -0.79$, -1.19, and -2.98 eV. The physical observables converge to the same value at high voltage V_0 regardless of U, which actually implies that at large V_0 the electron and hole are well separated and thus there is almost no on-site electrostatic energy contribution in E_b. Basically there are two characteristic behaviors, the regime of small band offset ($V_0 < 0.1$ eV) and large band offset ($V_0 > 0.4$ eV). This reflects the competition between Coulomb interaction and the

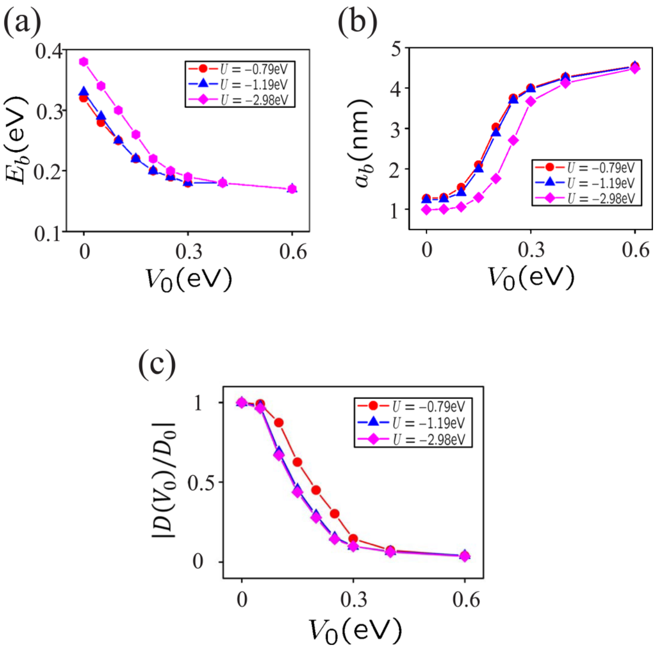

FIG. 2. (a) The binding energy E_b, (b) the exciton radius a_b, and (c) optical dipole ratio $|D(V_0)/D_0|$ versus the strength of the band offset V_0 for different on-site Coulomb potential U. The red sphere, blue triangle, and magenta diamond symbols, respectively, represent results for different on-site electrostatic energy $U = -0.79$, -1.19, and -2.98 eV. The physical observables converge to the same value at high voltage V_0 regardless of U, showing the spatial separation nature of the interface exciton for large V_0. There are two characteristic behaviors, in the regime of small band offset ($V_0 \ll 0.1$ eV) and large interface potential ($V_0 > 0.1$ eV), which reflects the competition between Coulomb interaction and the band offset. Here, D_0 is the value of $D(V_0)$ at $V_0 = 0$ (i.e., that of the 2D exciton in the absence of interface). See text for details.

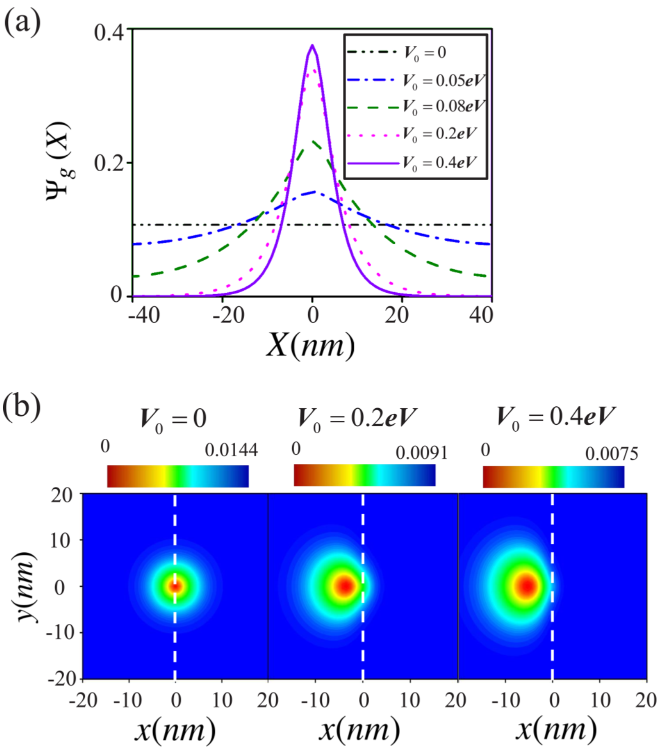

FIG. 3. (a) Center-of-mass wave function and (b) relative motion spatial probability distribution at different V_0. The white dashed line denotes the central position of the interface. From (a) we see that the wave function undergoes a transition from an extended state to a localized state as V_0 increases, demonstrating the competition between the Coulomb interaction and the band offset. From (b), we see that for larger V_0 the electron-hole pair tends to be farther apart and electron-hole overlap is greatly reduced.

band offset. For small band offset V_0, $V_C(r)$ dominates over $V_I(\mathbf{R}, \mathbf{r})$ so the exciton ground state is almost equivalent to a 2D exciton while $V_I(\mathbf{R}, \mathbf{r})$ is regarded as a perturbation term. Therefore, the physical observables of type-II interface exciton are almost the same as the ones for 2D exciton in this regime. However, for sufficiently large V_0, $V_I(\mathbf{R}, \mathbf{r})$ dominates over $V_C(r)$. The effective radius a_b shows a rapid rise while D drops dramatically as the band offset increases. In this sense, we can control physical properties of type-II interface exciton by adjusting the band offset.

We obtained an interface exciton binding energy of about 0.2 eV which is of the same order as a 2D exciton in TMDs. Such a large binding energy at a type-II interface is not present in most conventional semiconductor nanostructures [5,62,63]. In fact, a type-II interface exciton is often considered unstable in conventional semiconductor heterostructures [5,64] unless in the presence of other physical structures like an E field [64] or within a quantum dot [62]. In a TMD lateral heterojunction, however, with a relatively large binding energy a type-II interface exciton is predicted to be stable with our calculations. It is also of concern whether the interface exciton changes back to a 2D exciton easily. From Fig. 2(b) we see that at $V_0 = 0.2$ eV the binding energy of the interface exciton is about 0.22 eV, which is about 0.1 eV smaller than the binding energy of 2D exciton. In this sense, we may assume that for realistic configurations the interface exciton is a stable ground state of lateral heterojunctions. The relatively large binding energy exactly results from the weaker screening effect of Coulomb interaction when the electron-hole separation increases as shown in Eq. (2).

It is noted that for a large V_0 the on-site Coulomb interaction for an interface exciton is irrelevant. This implies that the electron and hole are well separated into opposite regions for sufficiently large V_0, while for small and intermediate V_0, even though qualitative behaviors are similar, numerical values obtained with different U are quite different. Without loss of generality, $U = -0.79$ eV is assumed in the remainder of the paper as it gives the closest free exciton E_b with Ref. [50] for 2D exciton.

The center-of-mass part $\Psi_g(X)$ and relative motion wave function with fixed electron position are, respectively, depicted in Figs. 3(a) and 3(b) for different V_0. From Fig. 3(a) we see how $\Psi_g(X)$ varies from $V_0 = 0$ to 0.4 eV. For small band offset $V_0 < 0.1$ eV $\Psi_g(X)$ is widespread across the supercell. This is expected since for small V_0 the electron-hole pair behaves as a 2D exciton. But for sufficiently high V_0, $\Psi_g(X)$ is localized around the interface at $X = 0$. The center-of-mass part of the wave function undergoes a transition from a plane wave to a localized state as V_0 increases, demonstrating

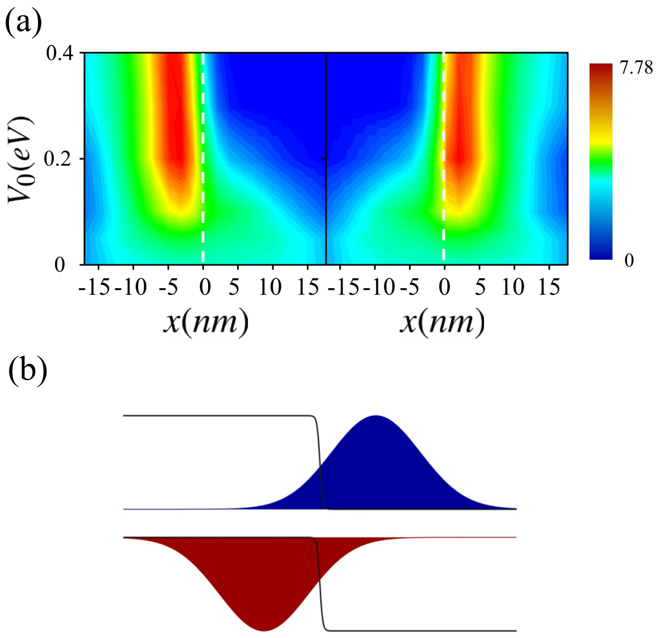

FIG. 4. (a) Left: hole, and right: electron reduced wave function versus V_0. Since the translational symmetry is preserved along the y direction, we only show the cross section of the reduced wave function along the x direction at $y = 0$. Apparently the electron-hole pair is effectively separated at high V_0. However, for $V_0 \sim$ 0.1–0.2 eV a finite tail into the barrier region remains which gives rise to a considerable electron-hole overlap. (b) Schematics of an interface exciton for $V_0 > 0.1$ eV. A considerable overlap between the electron and hole wave functions survives even for a great spatial separation of the electron and hole. Here, the thin lines denote the band offsets. The dark blue and dark red regions, respectively, denote the cross section of the electron and hole's reduced wave functions along the x direction at $y = 0$.

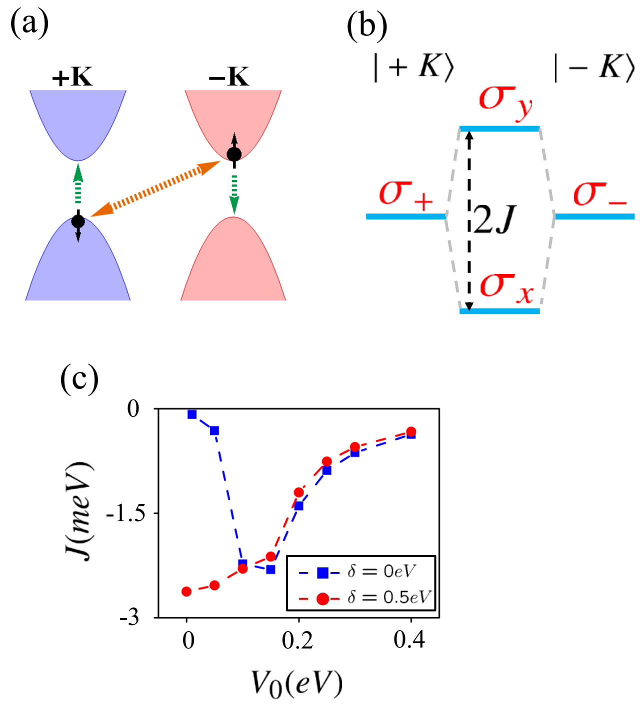

FIG. 5. (a) Illustration of the intervalley exchange interaction. Mediated by the exchange part of the Coulomb interaction (the orange arrow), the exciton may change their pesudospin from $-K$ to $+K$ as indicated by the green arrow, effectively resulting in a valley exchange channel. (b) The exchange interaction J leads to a splitting between the degenerate $\pm K$ states. The $\sigma_+, \sigma_-, \sigma_x, \sigma_y$, respectively, denotes the polarizations of the light fields which can pump the corresponding states. The x and y directions are shown in Fig. 1(a). (c) The valley coupling strength J versus V_0 for a symmetric and asymmetric heterojunction, respectively. Rotational symmetry requires vanishing J at $V_0 = 0$ for a symmetric heterojunction, in contrast to an asymmetric heterojunction for which J increases at low V_0. At high voltage valley coupling of an interface exciton is small regardless of symmetry of the heterojunction because of the reduced electron-hole overlap.

the competition between the Coulomb interaction and the band offset. From Fig. 3(b), the biased relative motion wave function for large V_0 implies that the electron-hole pair tends to be separated apart well and thus electron-hole overlap is greatly reduced. To further demonstrate the separation nature of the type-II interface exciton, the reduced wave function of the electron and hole versus V_0 is shown in Fig. 4(a), where obviously the electron preferentially stays at the left hand side of the interface while the hole stays at the right hand side of the interface.

There is still a considerable optical dipole because of the tunneling tail of the electron and hole reduced wave function. We find that a small but notable electron-hole overlap still survives. Such an electron-hole overlap can be schematically demonstrated by Fig. 4(b). The finite magnitude of overlap for $V_0 > 0.1$ eV implies that the optoelectrical properties can be still detected for interface exciton. From Fig. 2(c) we see that at $V_0 = 0.2$ eV, D only drops by half that of 2D excitons, and by one order of magnitude at 0.3 eV. Thus at such V_0 the interface exciton still can be excited by the pumping light. On the other hand, reduction of D suggests a longer lifetime. For very large V_0, D is a few orders smaller than 2D excitons, meaning that the interface exciton may have a lifetime far exceeding 2D excitons.

Finally we calculated the intervalley coupling strength J for different V_0 at $U = -0.79$ eV for both a symmetric interface with $\delta = 0$ and an asymmetric interface with $\delta = 0.5$ eV in Fig. 5. For the symmetric case, it is expected that J tends to zero for $V_0 = 0$ due to the emergence of threefold rotation symmetry. When V_0 increases, broken symmetry results in a dramatic increase of intervalley coupling. However for an asymmetric interface with $\delta = 0.5$ eV, the threefold rotation symmetry is broken at the beginning and thus there is a considerable J at $V_0 = 0$. However as V_0 further increases, the broken symmetry plays a minor role and a very similar monotonic decreasing behavior in J is observed for both interfaces. This manifests the reduced electron-hole overlap $\psi(P_X)$ as in the drop of D when V_0 increases.

A nonzero intervalley coupling between $\pm K$ implies that interface exciton ground state has a valley part of the form $\frac{1}{\sqrt{2}}(|K\rangle \pm |-K\rangle)$. This suggests that the interface exciton couples with linearly polarized light instead of circularly polarized light as in 2D excitons which is shown in Fig. 5(b). Our calculations show that J has an order of a few meV in Fig. 5(c).

Under current parameters, we have numerically evaluated the first and second order terms of a more rigorous generalized BOA [58,59] and find that even within the intermediate regime of V_0, the corrections terms are in the order 10^{-6} eV, which is much smaller than the energy level spacing in the order of 10^{-1} eV. Thus the correction terms may safely be neglected and the zeroth-order BOA is sufficient for current circumstance.

E. Numerical results based on continuous model

When the size of the supercell is much larger than the lattice constant, we can also introduce a continuous model of type II interface exciton, where its Hamiltonian in Eq. (6) is diagonalized with a 2D hydrogenic basis. In the Hilbert space expanded by the 2D hydrogenic basis $\{\phi_{nl}(r)\}(n=0,1,\dots,l=-n+1,\dots,n-1)$ which satisfy the Schrödinger equation of the usual 2D hydrogen atom [65]

$$\left(-\frac{\hbar^2}{2\mu}\nabla_{\mathbf{r}}^2-\frac{e^2}{\varepsilon r}\right)\phi_{nl}(r)=E_n\phi_{nl}(r), \tag{11}$$

Eq. (6) can be rewritten as

$$a_{nl}^k(X)[E(X)-E_k(X)]+\sum_{n'=1}^{\infty}\sum_{l'=-n+1}^{n-1}V_{n'l'}^{nl}(X)a_{n'l'}^k(X)=0, \tag{12}$$

where $\Theta_k(X,\mathbf{r})=\sum_{n,l}a_{nl}^k(X)\phi_{nl}(\mathbf{r})$ has already been assumed as the linear combination of the basis with coefficients $\{a_{nl}^k(X)\}$ and the elements of the electric potential are defined as $V_{n'l'}^{nl}(X)=\int d\mathbf{r}\phi_{nl}^*(\mathbf{r})[V_C(r)+V_I(X,\mathbf{r})]\phi_{n'l'}(\mathbf{r})$.

Since we need an infinite principal quantum number n to complete the Hilbert space of Eq. (6) which is obviously impossible, we need to set a cutoff n when both the binding energy and wave function of the ground state interface exciton are convergent. We plot the binding energy versus the principal number n for different potential strength V_0 in Fig. 6. It is obvious that the ground state energies converge very quickly along with the principal quantum number even for relatively large potential strength. In the following discussion, the cutoff of n is set to be $n_{\text{cutoff}}=7$. It is also important to note that the dielectric constant $\varepsilon\approx1.10\varepsilon_0$ for the 2D hydrogenic basis is fixed in the above numerical calculation in order to obtain the same binding energy $E_b\approx220$ meV as the one from the TB model at $V_0=0.2$ eV. Here, ε_0 is the vacuum dielectric constant. In this sense, the binding energy of the 2D exciton is $E_b=396$ meV. The other parameters are the same as those for the TB model. Based on the continuous model the numerical results of the binding energy E_b, effective radius a_b, and optical dipole ratio $|D(V_0)/D_0|$ obtained with different strength of the band offset V_0 are shown in Fig. 7 as the blue triangle symbols and solid lines. Here, the numerical results based on the TB model are also shown in the same figure as the red sphere symbols and dashed lines. The numerical results, especially the energies, resemble each other reasonably, which implies the validity of both methods. For large band offset V_0, the difference between the numerical results of both methods becomes greater because the size of the supercell we chose is not sufficiently large.

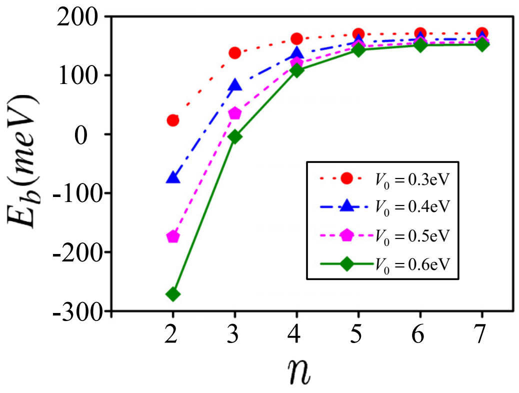

FIG. 6. The binding energy E_b versus the cutoff of principal quantum number n for different potential strength V_0. The dotted red line with circle symbol, dot-dashed blue line with triangle symbol, magenta short-dashed line with pentagon symbol, and olive solid line with diamond symbol represent the ground state energies with potential strength $V_0=0.3, 0.4, 0.5, 0.6$ eV, respectively. The other parameters are chosen as $\varepsilon\approx1.1\varepsilon_0$, $m_e=0.434m_0$, and $m_h=0.533m_0$ with vacuum dielectric constant ε_0 and free electron mass m_0. It is clear that the ground state energies converge very quickly along with increasing principal quantum number even for relative large potential strength.

F. Interface exciton at lateral double heterojunctions

The former discussion focuses on the properties of the 1D interface exciton at single heterojunction as shown in

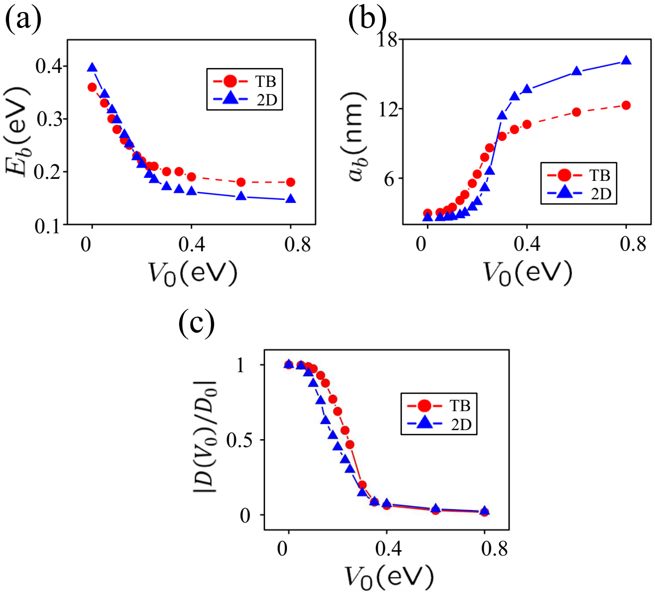

FIG. 7. (a) The binding energy E_b, (b) the exciton radius a_b, and (c) the optical dipole ratio $|D(V_0)/D_0|$ versus the strength of the band offset V_0. The blue triangle symbols with solid line and the red sphere symbols with dashed line, respectively, represent the numerical results obtained from the TB model and continuous model, which are respectively denoted as "TB" and "2D" in the plot.

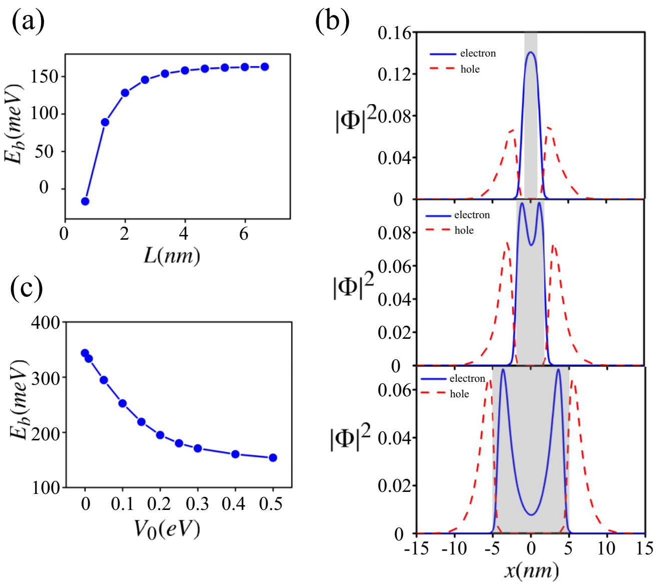

FIG. 8. (a) The binding energy of the interface exciton at lateral double heterojunctions versus the width of the double heterojunctions L. (b) The typical reduced wave function of electrons (blue solid lines) and holes (red dashed lines) for different widths of double heterojunctions. The three different widths are $L \approx 1.3$ nm, 3.3 nm, 10 nm. The corresponding central regions are denoted by the shadow areas. See text for the details. (c) The binding energy of the interface exciton versus the potential strength of the double heterojunctions V_0 for $L \approx 3.3$ nm.

Fig. 1(a). Another important case is the lateral double heterojunctions as shown in Fig. 1(d). When the interface exciton is generated in such a structure, the electron is supposed to locate at the central region and the hole is supposed to locate at both hands side of the central region due to the lattice potential. However, because of the Coulomb interaction the electron and the hole have a tendency to bind each other. Such competition will affect the properties of the interface exciton greatly. Since the lattice potential depends on the width of the double heterojunctions as well as the potential strength now, we calculate the binding energy of the interface exciton versus the width of the double heterojunctions L and the potential strength V_0 by applying the TB method.

The binding energy versus the width of the double heterojunctions L is depicted in Fig. 8(a). The V_0 is chosen as 0.5 eV in Fig. 8(a). The other parameters are chosen the same as those in Fig. 2. As shown in Fig. 8(a), the binding energy increases as the width of the double heterojunctions increases and eventually saturates to a constant value which is the binding energy of the 1D exciton shown in Fig. 2(a). It can be interpreted by the overlap of the 1D excitons locating at both interfaces. The reduced wave function of electron and hole for different widths of the double heterojunctions L are, respectively, depicted as blue solid lines and red dashed lines in Fig. 8(b). The typical effective radius of the 1D exciton for potential strength $V_0 = 0.5$ eV is around 5 nm as shown in Fig. 2(c). For a small double heterojunction with $L < 5$ nm, the lattice potential dominates the binding energy of the interface exciton. The consisting electron in 1D excitons locating at both interfaces has great overlap which results in that the electron can only locate at the very center of the double heterojunctions. When the double heterojunctions width increases to be larger than the typical effective radius of the 1D exciton such as $L > 5$ nm, the Coulomb interaction becomes dominating and the electron prefers to locate in the vicinity of each interface which actually reduces the overlap of the electrons wave function. When the width L is much larger than the effective radius, the overlap tends to zero which results in the saturated value equaling to the binding energy of the 1D interface exciton.

The binding energy versus the potential strength V_0 is depicted in Fig. 8(c), where L is chosen as 1.3 nm. The binding energy decreases when the potential strength V_0 increases. The reason is that the effective radius of the 1D interface exciton becomes larger as the potential strength V_0 increases as shown in Fig. 2(b). Therefore the overlap of the electron wave function becomes smaller and eventually reduces the binding energy.

IV. INTERFACE EXCITON AT CLOSED TRIANGULAR SHARP INTERFACE AND EFFECTIVE QUANTUM DOT CONFINEMENT

A. Numerical results of closed triangular sharp interface without valley index

For all the discussion above, we have assumed the quasi-1D heterojunction as shown in Fig. 1. However, the realistic lateral heterostructures for TMDs present the triangular shape [29–32], whose characteristic length scale is about 5 μm. Usually, the electron-hole separation of the interface exciton is up to 10 nm for large V_0 from the above calculation of the 1D interface. It is much smaller than the characteristic length scale of triangular heterostructures, which means the calculation of 1D interface is also valid for the closed triangular sharp interface in current experiments.

If the characteristic length scale of closed triangular sharp interface decreases to the same order of the electron-hole separation of interface exciton, the electron (hole) wave function will be strongly affected by the boundaries of the triangular shape and thus such quantum confinement effect should be taken into consideration. Actually, such closed triangular interface effectively realizes 0D quantum dot confinement of the interface excitons. From the similar Hamiltonian in Eq. (1) but with triangular band offset as shown in Fig. 9, which reads

$$V_{\rm e}(\mathbf{r}) = \begin{cases} V_0, & \mathbf{r} \in \text{triangular quantum dot}, \\ 0, & \mathbf{r} \notin \text{triangular quantum dot}, \end{cases} \tag{13}$$

$$V_{\rm h}(\mathbf{r}) = \begin{cases} 0, & \mathbf{r} \in \text{triangular quantum dot}, \\ V_0, & \mathbf{r} \notin \text{triangular quantum dot}. \end{cases} \tag{14}$$

Here, $L_{\rm SC}$ and $W_{\rm SC}$ are the length and the width of the supercell adopted in the calculations in units of lattice constant a, and R is the edge length of the regular triangular quantum dot. If $V_0 < 0$, the electron is confined in the triangular quantum dot while the hole stays in the proximity exterior. In contrast, when $V_0 > 0$, the hole is confined in the triangular quantum dot while the electron stays in the proximity exterior. We consider the scenario $V_0 < 0$ in the following discussion. For $V_0 > 0$, our calculation of the envelop function based on the effective mass approximation and one-band tight-binding

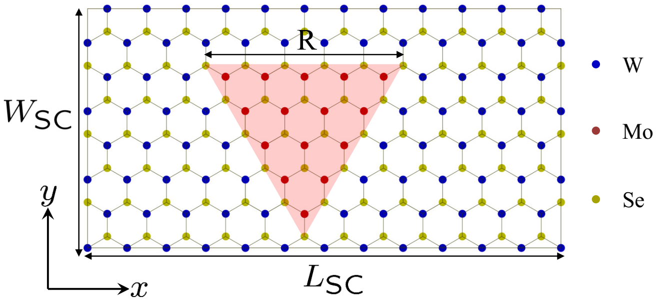

FIG. 9. Schematics of the triangular heterostructure formed by monolayer $WSe_2 - MoSe_2$. The blue, red, and yellow spheres, respectively, denote W atoms, Mo atoms, and Se atoms. The red shadow region denotes the region of triangular band offset.

model can be applied by simply swapping the electron and hole masses.

Since the translational symmetry is no longer preserved in such a closed triangular sharp interface, we need to develop another numerical method to calculate the physical properties of the interface exciton. The complete orthonormal basis $\{\phi_e^{(n)}(\mathbf{r}_e)\otimes\phi_h^{(n,m)}(\mathbf{r}_h)\}$ is introduced to expand the original Hamiltonian, where $\phi_e^{(n)}(\mathbf{r}_e)$ is the nth eigenstate of the electron confined in the triangular region without hole part such as

$$\left[-\frac{\hbar^2}{2m_e}\nabla^2_{\mathbf{r}_e} + V_e(\mathbf{r}_e)\right]\phi_e^{(n)}(\mathbf{r}_e) = E_e^{(n)}\phi_e^{(n)}(\mathbf{r}_e), \qquad (15)$$

and the $\phi_h^{(n,m)}(\mathbf{r}_h)$ is the mth eigenstate of the hole effective Hamiltonian $H_{\text{eff}}^{(n)}(\mathbf{r}_h)\phi_h^{(n,m)}(\mathbf{r}_h) = E_h^{(n,m)}\phi_h^{(n,m)}(\mathbf{r}_h)$, where the effective Hamiltonian of hole is obtained by averaging the original Hamiltonian on $\phi_e^{(n)}(\mathbf{r}_e)$ as

$$H_{\text{eff}}^{(n)}(\mathbf{r}_h) = \int d\mathbf{r}_e \phi_e^{(n),*}(\mathbf{r}_e) H \phi_e^{(n)}(\mathbf{r}_e). \qquad (16)$$

It should be indicated that not only the confined states of electron with energies less than V_0 but also the propagating states with energies larger than V_0 are taken into consideration to guarantee the completeness of the orthonormal basis. The Hamiltonian matrix elements are straightforwardly calculated as

$$H_{n,m}^{n',m'} \equiv \int d\mathbf{r}_e \int d\mathbf{r}_h \phi_e^{(n'),*}(\mathbf{r}_e)\phi_h^{(n',m'),*}(\mathbf{r}_h) H \times \phi_e^{(n)}(\mathbf{r}_e)\phi_h^{(n,m)}(\mathbf{r}_h), \qquad (17)$$

which can be simplified according to the orthogonality of the basis as

$$H_{n,m}^{n',m'} = \begin{cases} E_e^{(n)} + E_h^{(n,m)}, & \text{if } n = n' \text{and } m = m', \\ 0, & \text{if } n = n' \text{and } m \neq m', \\ V_C(n, n', m, m'), & \text{if } n \neq n', \end{cases} \qquad (18)$$

with

$$V_C(n, n', m, m') \equiv \int d\mathbf{r}_e \int d\mathbf{r}_h \phi_e^{(n'),*}(\mathbf{r}_e)\phi_h^{(n',m'),*}(\mathbf{r}_h) \times V_C(|\mathbf{r}_e - \mathbf{r}_h|)\phi_e^{(n)}(\mathbf{r}_e)\phi_h^{(n,m)}(\mathbf{r}_h). \qquad (19)$$

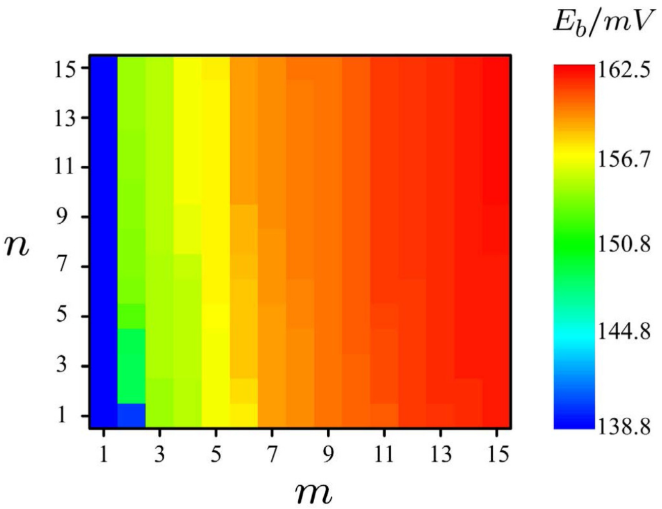

FIG. 10. The binding energy of the exciton of the closed triangular interface E_b versus the quantum number m and n. The parameters are chosen as $R = 30a$, $L_{SC} = 60a$, $W_{SC} = 36\sqrt{3}a$, $V_0 = 0.3$ eV. The binding energy converges quickly along the quantum numbers. In the following calculation, we set the same cutoff $n_{\text{cutoff}} = m_{\text{cutoff}} = 15$ for different V_0.

We solve the eigenproblem by diagonalizing the Hamiltonian matrix. We still need to set a cutoff for n and m when the binding energy of the ground state interface exciton is convergent. As shown in Fig. 10, where the parameters are chosen as $R = 30a$, $L_{SC} = 60a$, $W_{SC} = 36\sqrt{3}a$, $V_0 = 0.3$ eV, clearly the binding energy converges quickly along the quantum numbers, especially along n. In the following calculation, we set the same cutoff $n_{\text{cutoff}} = m_{\text{cutoff}} = 15$ for different V_0.

The numerical results of the binding energy versus the band offset V_0 and the size of the quantum dot R is depicted in Fig. 11. The binding energy monotonically decreases as the band offset increases as shown in Fig. 11(a), which results from the stronger quantum confinement. However, as shown in Fig. 11(b), the behavior of the binding energy versus R has a maximum value due to the competition between the quantum confinement and the Coulomb interaction. When $R < 30a$, basically the ground state of the electron and hole dominates the wave function, and thus when R increases to

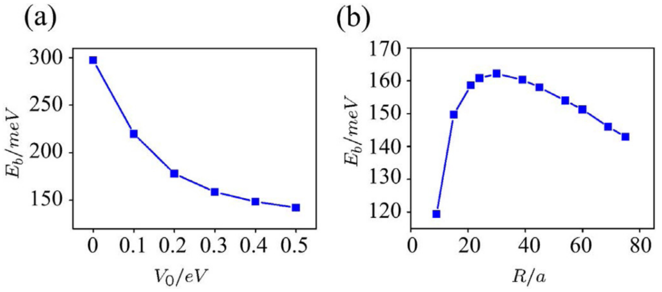

FIG. 11. The binding energy versus (a) the band offset V_0 and (b) the size of the quantum dot R. The parameters for (a) are chosen as $R = 21a$. The potential strength is chosen as $V_0 = 0.3$ eV. The size of the supercell is sufficiently large.

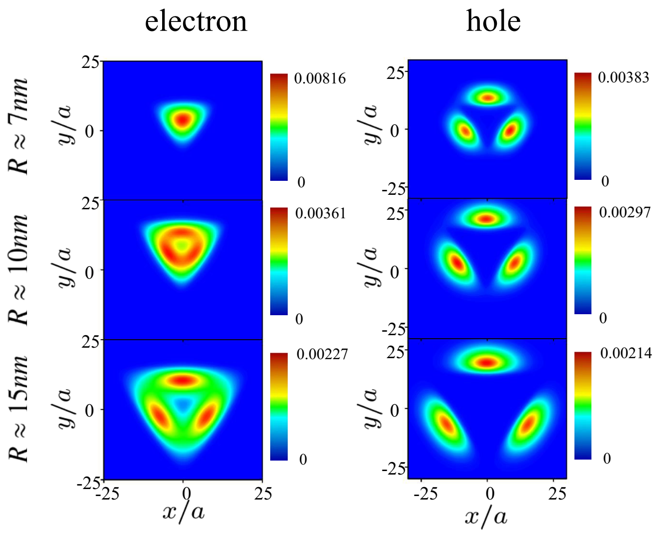

FIG. 12. The reduced wave function of the electron (left panel) and hole (right panel) for closed triangular interface with different sizes $R = 21a, 30a, 45a$, namely $R \approx 7$ nm, 10 nm, 15 nm from the top to bottom. The potential strength is chosen as $V_0 = 0.3$ eV.

decrease the quantum confinement, the binding energy of exciton increases. While when $R > 30a$, the excited states of electron and hole start to appear in the wave function, which results in the decrement of binding energy. So if such decrement is greater than the increment of binding energy resulting from quantum confinement, the binding energy of exciton decreases as the size of quantum dot R increases. Therefore, there is a maximum binding energy for an optimal R.

Such competition can be also demonstrated in the reduced wave function of the electron and hole as shown in Fig. 12. The left and right panels, respectively, show the reduced wave function of electron and hole for increasing size of the quantum dot from the top to bottom. All reduced wave functions have the threefold rotation symmetry inheriting from the symmetry of the regular triangular shape of the closed interface. For a small quantum dot such as $R = 21a$, the electron is strongly confined in the quantum dot and the hole wave function stays in the proximity exterior of the quantum dot. While for a large quantum dot such as $R = 45a$, the wave functions of electron and hole only spread over the vicinity of the edges of the closed interface. Without the interplay between the wave functions at different edges, the closed triangular interface will degrade to the 1D interface case. For a large quantum dot, the binding energy is about 140 meV, which is consistent with the former 1D interface calculation as shown in Fig. 2(a).

We can imagine that when the size of the quantum dot is much larger than the effective radius of the 1D interface exciton, which is about 5 nm according to the previous calculation, the interface exciton actually is split into three identical parts locating at the edges of triangular quantum dot and each part is analogy to the quasi-1D exciton. When the size of the triangular quantum dot is decreased, the three parts have considerable overlap at the corners of the triangular quantum dot when the size of the triangular quantum dot decreases. In this sense, an effective Hamiltonian is introduced to describe such a threefold rotational symmetric system as

$$H_{\text{eff}} = \begin{bmatrix} E_0 & te^{i\theta} & te^{-i\theta} \\ te^{-i\theta} & E_0 & te^{i\theta} \\ te^{i\theta} & te^{-i\theta} & E_0 \end{bmatrix} \tag{20}$$

with bases $\{|\Phi\rangle, C_3|\Phi\rangle, C_3^2|\Phi\rangle\}$. Here, $|\Phi\rangle$ is the wave function of 1D interface exciton at one edge, C_3 and C_3^2 are rotation operators of threefold rotational group, E_0 is the binding energy, and $te^{i\theta}$ represents the transition between wave functions of 1D interface exciton at different edges. In order to satisfy the threefold rotation symmetry, the phase factor can only be $\theta = 0, \frac{2\pi}{3}$, or $\frac{4\pi}{3}$. In addition, the phase factors for the opposite valley should be opposite according to the time-reversal symmetry. Both binding energy E_0 and transition coefficient t are determined by the numerical calculation based on the excitonic lattice model.

By diagonalizing the effective Hamiltonian, the lowest three excitonic states can be found as

$$|\phi_1\rangle = \frac{1}{\sqrt{3}}\big(e^{i\pi}|\Phi\rangle + e^{i\frac{\pi}{3}}C_3|\Phi\rangle + e^{i\frac{5\pi}{3}}C_3^2|\Phi\rangle\big), \tag{21}$$

$$|\phi_2\rangle = \frac{1}{\sqrt{3}}\big(|\Phi\rangle + e^{i\frac{2\pi}{3}}C_3|\Phi\rangle + e^{i\frac{4\pi}{3}}C_3^2|\Phi\rangle\big), \tag{22}$$

$$|\phi_3\rangle = \frac{1}{\sqrt{3}}\big(|\Phi\rangle + C_3|\Phi\rangle + C_3^2|\Phi\rangle\big), \tag{23}$$

with corresponding eigenenergies $E_i = E_0 + 2t\cos(\frac{2i\pi}{3} - \theta)$ $(i = 1,2,3)$. Since θ can only be $0, \frac{2\pi}{3}$, or $\frac{4\pi}{3}$, there are two degenerate states. We take $\theta = -2\pi/3$ for $\tau = 1$ as an example. The energy level scheme is depicted in Fig. 13(a), where obviously $|\phi_1\rangle$ and $|\phi_3\rangle$ are degenerate states. A more interest fact is that there is a transition when the absolute value of the transition coefficient t varies from a negative value to a positive one. When $t < 0$, the $|\phi_2\rangle$ is ground state. In contrast, when $t > 0$, the degenerate states $|\phi_1\rangle$ and $|\phi_3\rangle$ become ground states.

Such a transition is depicted in Fig. 13(a). The numerical calculation based on the lattice model shows the transition occurs when the size of the triangular quantum dot is about 12.5 nm [Fig. 13(b)]. The transition coefficient t can also be parameterized by the numerical calculation, which is shown in Fig. 13(c). The absolute value of transition coefficient t strongly depends on the overlap of the quasi-1D excitonic wave functions at the corners of the triangular quantum dot. For a small quantum dot, the electron confined in the quantum dot and thus the overlap of the electron part supplies a relatively large attractive Coulomb interaction to overcome the kinetic energy. Therefore t has negative value. In contrast for a large quantum dot, both the electron and hole spread over the vicinity of the edges of the quantum dot, and thus the overlap of the electron and hole are greatly decreased. In this sense, the Coulomb interaction part becomes smaller than the kinetic part resulting in positive t.

Among the above three excitons, only one state is a bright exciton and the other two states are dark excitons when pumping them with right (σ_+) or left (σ_-) circularly polarized light. The optical transition matrix elements of those excitons are proportional to $\langle\phi_i|P_\pm|vac\rangle$, $(i = 1, 2, 3)$, where $P_\pm$ are the dipole moments corresponding to the σ_+ or σ_- circularly

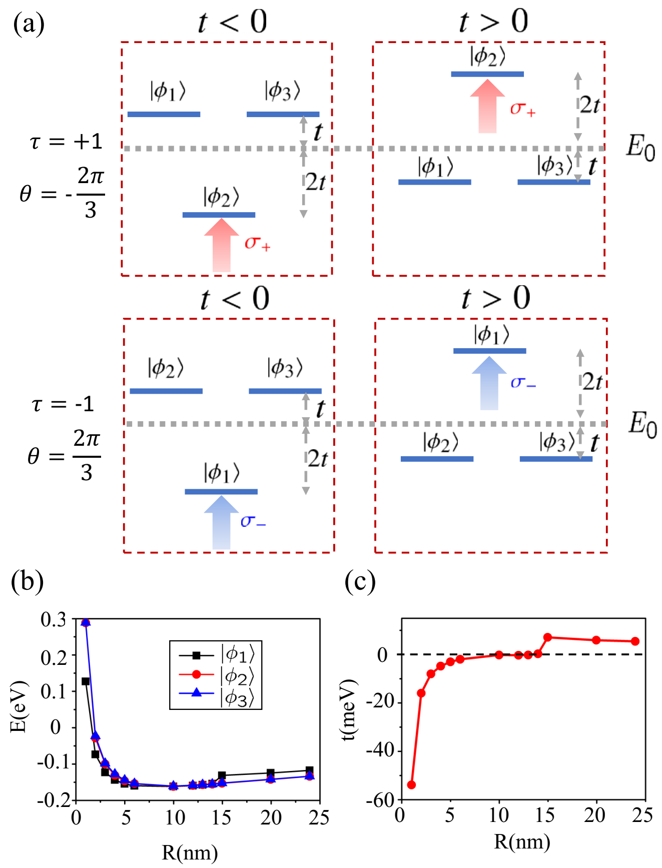

FIG. 13. (a) The energy level schemes for $t < 0$ and $t > 0$ when $\theta = \mp 2\pi/3$ for $\tau = \pm 1$ valleys. The optical selection rules are also depicted. Here, $\tau = \pm 1$ are valley index denoting K and $-K$ valleys. The light red and light blue arrows, respectively, denote the right (σ_+) and left (σ_-) polarizations of the light fields coupling to the corresponding exciton states. (b) The numerical results of the eigenenergies E and (c) the absolute value of the transition coefficient t versus the size of the triangular quantum dot R. Obviously, there is a transition when the ground state varies from a nondegenerate state to a degenerate one. Additionally, the transition coefficient changes from a negative value to a positive one.

polarized light and $|vac\rangle$ denotes the initial states with full valence bands and empty conduction bands. Since under the threefold rotation the transformations of the dipole moments are

$$C_3^{-1}P_\pm C_3 = e^{\pm i\frac{2\pi}{3}}P_\pm,\ (C_3^2)^{-1}P_\pm C_3^2 = e^{\pm i\frac{4\pi}{3}}P_\pm, \tag{24}$$

only the exciton states with appropriate phase factors of coefficients have nonzero optical transition matrix elements and thus are bright excitons. In this sense, the σ_- circularly polarized light can pump the $|\phi_1\rangle$ in the $\tau = -1$ valley, and σ_+ circularly polarized light can pump the $|\phi_2\rangle$ in the $\tau = +1$ valley. The corresponding optical selection rule is shown in Fig. 13(a).

B. Numerical results of closed triangular sharp interface with valley index

In the above discussion, only the interface excitons in the same valley are discussed. However, due to the geometry of the closed triangular sharp interface, the intervalley couplings are inevitable which eventually couple interface excitons in the opposite valleys. We start from the effective Hamiltonian both including the threefold rotational symmetric excitons and the intervalley couplings as

$$H_{\rm eff}^{\rm inter} = \begin{bmatrix} E_0 & te^{i\theta_+} & te^{-i\theta_+} & p & q & q \\ te^{-i\theta_+} & E_0 & te^{i\theta_+} & q & p & q \\ te^{i\theta_+} & te^{-i\theta_+} & E_0 & q & q & p \\ p & q & q & E_0 & te^{i\theta_-} & te^{-i\theta_-} \\ q & p & q & te^{-i\theta_-} & E_0 & te^{i\theta_-} \\ q & q & p & te^{i\theta_-} & te^{-i\theta_-} & E_0 \end{bmatrix}, \tag{25}$$

where the bases in the real space ($i = 1, 2, 3$) are

$$\langle \mathbf{r_e}, \mathbf{r_h}|\phi_i, \tau\rangle \approx \exp\left(i\tau\mathbf{K}\cdot(\mathbf{r_e}-\mathbf{r_h})\right)\langle \mathbf{r_e}, \mathbf{r_h}|\phi_i\rangle \times u_{\mathbf{K}}(\mathbf{r_e}, \mathbf{r_h}) \tag{26}$$

and $\tau = \pm 1$ is the valley index. The $|\phi_i\rangle$ are the envelopes of the excitonic states without considering the valley index which are defined in Eqs. (21)–(23) and $u_{\mathbf{K}}(\mathbf{r_e}, \mathbf{r_h})$ is the periodic parts of the Bloch wave functions. We adopted the assumption that $u_{\mathbf{K}+\mathbf{q}}(\mathbf{r_e}, \mathbf{r_h}) \approx u_{\mathbf{K}}(\mathbf{r_e}, \mathbf{r_h})$ for the sake of simplicity. Here, $E_0 = \langle \phi_i, \tau|H|\phi_i, \tau\rangle$ is the binding energy of the 1D interface exciton, $t = \langle \phi_i, \tau|HC_3|\phi_i, \tau\rangle$ is the intravalley interedge hoppings, $p = \langle \phi_i, \tau|H|\phi_i, \overline{\tau}\rangle$ is the intervalley intraedge hoppings, and $q = \langle \phi_i, \tau|HC_3|\phi_i, \overline{\tau}\rangle$ is the intervalley interedge hoppings. Here, the original Hamiltonian H is introduced in Eq. (1). In order to make sure that the ground state of the interface exciton still inherits the same optical selection rule, which means that the σ_+ (σ_-) circularly polarized light only pumps the ground states of the excitons in the $\tau = +1$ ($\tau = -1$) valley, the phase factors for both valleys are fixed as $\theta_+ = -\theta_- = -2\pi/3$.

Since the intervalley terms $p(q)$ are at least one order smaller than the corresponding intravalley terms $E_0(t)$ due to the large momentum difference, and the intervalley terms result from the wave-function overlap at the corners which obviously become smaller when the size of the quantum dot increases, the magnitudes of the parameters have the following relations $E_0 \gg t \sim p \gg q$. In the following calculation, we ignore the intervalley interedge hoppings q. The numerical results of the intervalley intraedge hopping p versus the size of quantum dot R is shown in Fig. 14. The magnitude of p almost decreases exponentially as the size of the quantum dot increases. For the large quantum dot, the value matches the previous intervalley coupling results shown in Fig. 5 because the interface exciton degrades to a 1D interface exciton without the wave-function overlap at the corners. For a small quantum dot such as $R < 5$ nm it can reach to several meV.

Although q is small in comparison with t, it can still couple the interface excitons in opposite valleys. By diagonalizing the effective Hamiltonian $H_{\rm eff}^{\rm inter}$ in Eq. (25), we can obtain the lowest six interface excitonic states as

$$|\Phi_1\rangle = \cos\psi|\phi_2, \tau\rangle + \sin\psi|\phi_3, \overline{\tau}\rangle, \tag{27}$$

$$|\Phi_2\rangle = \cos\psi|\phi_1, \overline{\tau}\rangle + \sin\psi|\phi_3, \tau\rangle, \tag{28}$$

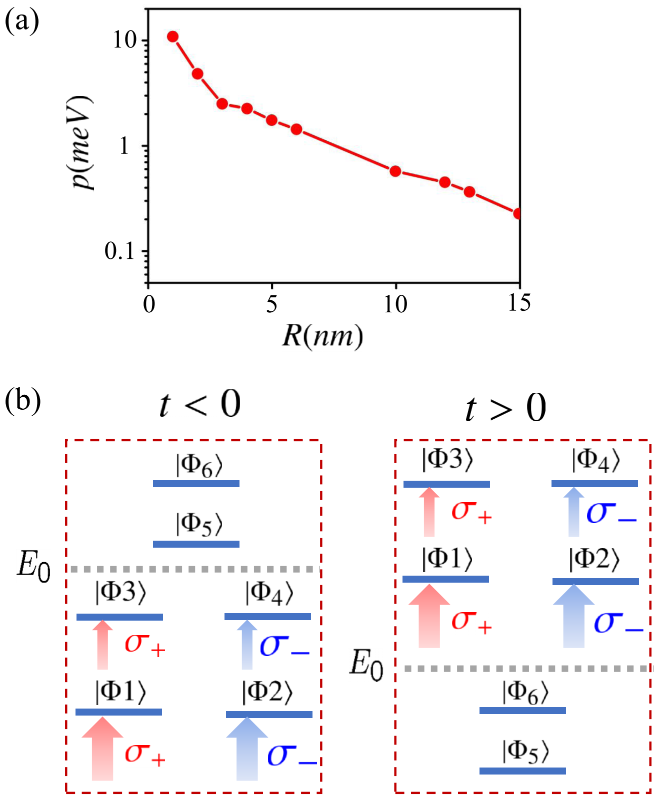

FIG. 14. (a) The intervalley intraedge hopping p versus the size of quantum dot R. The magnitude of p almost decreases exponentially as the size of the quantum dot increases. (b) The energy level schemes for $t < 0$ and $t > 0$ for $\theta_+ = -\theta_- = -2\pi/3$. The optical selection rules are also depicted. The light red and light blue arrows, respectively, denote the right (σ_+) and left (σ_-) polarizations of the light fields coupling to the corresponding exciton states. The different sizes of the arrows denote the coupling strengths between the exciton states and the light field.

$$|\Phi_3\rangle = -\sin\psi|\phi_2, \tau\rangle + \cos\psi|\phi_3, \overline{\tau}\rangle, \tag{29}$$

$$|\Phi_4\rangle = -\sin\psi|\phi_1, \overline{\tau}\rangle + \cos\psi|\phi_3, \tau\rangle, \tag{30}$$

$$|\Phi_5\rangle = \frac{1}{\sqrt{2}}(|\phi_1, \tau\rangle - |\phi_2, \overline{\tau}\rangle), \tag{31}$$

$$|\Phi_6\rangle = \frac{1}{\sqrt{2}}(|\phi_1, \tau\rangle + |\phi_2, \overline{\tau}\rangle), \tag{32}$$

with $\tan\psi = 2p/(3t)$ and the corresponding energies $E_1 = E_2 = E_0 + \frac{1}{2}(t - \sqrt{9t^2 + 4p^2})$, $E_3 = E_4 = E_0 + \frac{1}{2}(t + \sqrt{9t^2 + 4p^2})$, $E_5 = E_0 - t - p$, and $E_6 = E_0 - t + p$. Since the intervalley coupling p actually couples one bright exciton and one dark exciton such as $|\phi_2, \tau\rangle$ and $|\phi_3, \overline{\tau}\rangle$, both the $|\Phi_1\rangle$ and $|\Phi_3\rangle$ become bright but with different coupling strength with the same right circularly polarized light field. The energy level and the complete optical selection rule are shown in Fig. 14(b). According to the orthogonality of the periodic parts of the Bloch wave functions, the envelope wave function of the six excitonic states with the valley index are analogous to the wave function without the valley index shown in Fig. 12.

V. CONCLUSION

In this paper, we theoretically study the interface exciton states at various lateral heterojunctions of monolayer semiconductors including single, double, and closed triangular interfaces. When taking the distance dependent screening of Coulomb interaction into consideration, we numerically study the physical observables of the type II interface exciton including the binding energy, effective radius between the electron and hole, and optical dipole. Usually, such a problem is quite difficult to be numerically solved by *ab initio* calculations. We adopted two different approaches to calculate excitons. One approach bases on a real-space tight-binding model, and the other approach considers the perturbation expansion in a hydrogenlike basis in an effective mass model. The numerical study shows that even when the electron-hole separation is much larger compared to the 2D excitons in TMDs, the type II interface exciton still has strong binding energy. When the effective radius between the electron and the hole is up to four times of the Bohr radius of 2D excitons, the binding energy remains 1/2 that of 2D excitons. This can be interpreted by the weaker screening of Coulomb interaction as the electron-hole spatial separation increases. Large energy separation between the interface exciton and 2D excitons for band offset above 0.2 eV ensures that such 1D interface excitons are stable ones. Due to the spatial indirect nature of the type II interface exciton, exciton radius increases while optical transition dipole decreases as band offset increases. Still, the optical dipole is comparable to that of 2D excitons at a moderate band offset of 100 meV or below. Intervalley coupling that arises from electron-hole exchange is also studied, which may lead to the longitudinal-transverse splitting with the interface breaking the rotational symmetry. The lateral heterojunctions with closed triangular interface is also studied, which realizes the 0D quantum dot confinement of exciton. The numerical study shows that the energy level schemes and valley optical selection rules of the exciton in a quantum dot depends on the size of the quantum dot. Together with valley index, there are more exciton states in a single quantum dot which can be used to carry information. With its unique nature of having one carrier confined within the triangle by the band offset and the other carrier bounded to the proximity exterior of the triangle by the strong Coulomb, it is possible to realize the strong excitonic coupling between the neighboring quantum dots for mediating controlled interplay between spins at different dots [66]. In this sense, our investigation may facilitate the quantum information procession based on the 2D monolayer semiconductors.

ACKNOWLEDGMENTS

The work is mainly supported by the Research Grant Council of Hong Kong (HKU705513P, C7036-17W), and the Croucher Foundation. Z.R.G. is supported by NSFC Grant No. 11504241.

APPENDIX: GENERALIZED BORN-OPPENHEIMER APPROXIMATION

The regular Born-Oppenheimer approximation only consider the lowest order of the ratio between the reduced mass and the total mass $\kappa = \mu/M$ which corresponds to the relative motion and the center-of-mass motion, respectively. The total wave function is expressed as a product of the relative and center-of-mass parts when the adiabatic condition is satisfied. However, in the problem of our interface exciton there exist nonadiabatic processes and higher order terms in the ratio κ should be taken into consideration. In this sense, we present the generalized Born-Oppenheimer approximation and the corresponding second-order perturbation theory here.

The Schrödinger equation satisfied by one center-of-mass motion and multiple relative motions is $H\Phi(\mathbf{R},\{\mathbf{r}\}) = E\Phi(\mathbf{R},\{\mathbf{r}\})$ with Hamiltonian

$$H = -\frac{\hbar^2}{2M}\nabla_{\mathbf{R}}^2 + H(\{\mathbf{r}\}) + V(\mathbf{R},\{\mathbf{r}\}), \tag{A1}$$

where the first term is the kinetic energy of the center-of-mass motion, the second term describes the energy of the multiple relative motions $\{\mathbf{r}\} = \mathbf{r}_1, \mathbf{r}_2, \ldots$, and the third term is coupling between the center-of-mass motion and the relative motions. For arbitrary center-of-mass space coordinate $\mathbf{R}$, the eigenvalue equation

$$[H(\{\mathbf{r}\}) + V(\mathbf{R},\{\mathbf{r}\})]\Theta_k(\mathbf{R},\{\mathbf{r}\}) = E_k(\mathbf{R})\Theta_k(\mathbf{R},\{\mathbf{r}\}) \tag{A2}$$

can be solved to obtain the corresponding eigenvalues $E_k(\mathbf{R})$ and eigenfunctions $\Theta_k(\mathbf{R},\{\mathbf{r}\})$. Since these bases $\{\Theta_k(\mathbf{R},\{\mathbf{r}\})\}$ are orthogonal and complete, one expands $\Phi(\mathbf{R},\{\mathbf{r}\})$ in bases $\{\Theta_k(\mathbf{R},\{\mathbf{r}\})\}$ as

$$\Phi(\mathbf{R},\{\mathbf{r}\}) = \sum_{k=1}^{\infty}\Psi_k(\mathbf{R})\Theta_k(\mathbf{R},\{\mathbf{r}\}). \tag{A3}$$

Obviously, this expanded wave function satisfies the original Schrördinger equation as well. The straightforward derivation gives the set of the effective motion equations of the coefficients $\Psi_k(\mathbf{R})$ as

$$H_k(\mathbf{R})\Psi_k(\mathbf{R}) + \sum_{k'} H^1_{k,k'}(\mathbf{R})\Psi_{k'}(\mathbf{R}) = E\Psi_k(\mathbf{R}), \tag{A4}$$

where

$$H_k(\mathbf{R}) = H_k^0(\mathbf{R}) + H_k^1(\mathbf{R}), \tag{A5}$$

$$H_k^0(\mathbf{R}) = -\frac{\hbar^2}{2M}(\nabla_{\mathrm{R}} - i\mathbf{A}_{k,k}(\mathbf{R}))^2 + E_k(\mathbf{R}), \tag{A6}$$

$$H_k^1(\mathbf{R}) = \sum_{k'\neq k}\frac{\hbar^2}{2M}\mathbf{A}_{k,k'}(\mathbf{R})\cdot\mathbf{A}_{k',k}(\mathbf{R}), \tag{A7}$$

$$\begin{aligned} H^1_{k,k'}(\mathbf{R}) = {} & i\frac{\hbar^2}{M}\sum_{k'\neq k}\mathbf{A}_{k,k'}(\mathbf{R})\cdot\nabla_{\mathrm{R}}\Psi_{k'}(\mathbf{R}) \\ & + i\frac{\hbar^2}{2M}\sum_{k'\neq k}\int d\mathbf{r}[\nabla_{\mathrm{R}}\cdot\mathbf{A}_{k,k'}(\mathbf{R})]\Psi_{k'}(\mathbf{R}) \\ & + \frac{\hbar^2}{2M}\sum_{k'\neq k,k''}\mathbf{A}_{k,k''}(\mathbf{R})\cdot\mathbf{A}_{k'',k'}(\mathbf{R})\Psi_{k'}(\mathbf{R}), \end{aligned} \tag{A8}$$

and the Berry connections are defined as $\mathbf{A}_{k,q}(\mathbf{R}) \equiv i\int d\mathbf{r}\Theta_k^*(\mathbf{R},\{\mathbf{r}\})\nabla_{\mathrm{R}}\Theta_q(\mathbf{R},\{\mathbf{r}\})$. So far the effective motion equations are rigorous without any approximation. Here, the $H_k^0(\mathbf{R})$ and $H_k^1(\mathbf{R})$ are adiabatic terms because they only involve the kth energy level. However, $H^1_{k,k'}(\mathbf{R})$ involve the transitions between different energy levels introducing the nonadiabatic processes.

To obtain the explicit expression for $\mathbf{A}_{k,q}(\mathbf{R})$, differentiating the eigenvalue equation as Eq. (A2) leads to

$$\begin{aligned} &[H(\{\mathbf{r}\}) + V(\mathbf{R},\{\mathbf{r}\}) - E_p(\mathbf{R})]\nabla_{\mathrm{R}}\Theta_p(\mathbf{R},\{\mathbf{r}\}) \\ &\quad = [\nabla_{\mathrm{R}}E_p(\mathbf{R}) - \nabla_{\mathrm{R}}V(\mathbf{R},\{\mathbf{r}\})]\Theta_p(\mathbf{R},\{\mathbf{r}\}). \end{aligned} \tag{A9}$$

Multiplying $\Theta_k^*(\mathbf{R},\{\mathbf{r}\})$ to both sides of the above equation and integrating over all relative space coordinates $\{\mathbf{r}\}$ gives

$$\begin{aligned} &[E_k(\mathbf{R}) - E_p(\mathbf{R})]\int d\mathbf{r}\Theta_k^*(\mathbf{R},\{\mathbf{r}\})\nabla_{\mathrm{R}}\Theta_p(\mathbf{R},\{\mathbf{r}\}) \\ &\quad = -\int d\mathbf{r}\Theta_k^*(\mathbf{R},\{\mathbf{r}\})\nabla_{\mathrm{R}}V(\mathbf{R},\{\mathbf{r}\})\Theta_p(\mathbf{R},\{\mathbf{r}\}). \end{aligned} \tag{A10}$$

According to the definition of the Berry connection, the explicit expression of the absolute value of the Berry connections is

$$|\mathbf{A}_{k,p}(\mathbf{R})| = \left|\frac{\int d\mathbf{r}\Theta_k^*(\mathbf{R},\{\mathbf{r}\})[\nabla_{\mathbf{R}}V(\mathbf{R},\{\mathbf{r}\})]\Theta_p(\mathbf{R},\{\mathbf{r}\})}{E_k(\mathbf{R}) - E_p(\mathbf{R})}\right|. \tag{A11}$$

It is clear that the $H_k^1(\mathbf{R})$ and $H^1_{k,k'}(\mathbf{R})$ are regarded as the perturbations when the partial derivation of the coupling $\nabla_{\mathbf{R}}V(\mathbf{R},\{\mathbf{r}\})$ is much smaller than the energy level spacing $|E_k(\mathbf{R}) - E_p(\mathbf{R})|$. The order of the perturbations can be characterized by the number of the Berry connections. In this sense $H_k^1(\mathbf{R})$ is the second order perturbation and $H^1_{k,k'}(\mathbf{R})$ contains both the first order and the second order perturbations.

The Berry connections $\mathbf{A}_{k,k}(\mathbf{R})$ in the $H_k^0(\mathbf{R})$ actually play the role of a gauge field. It is important to indicate that for Eq. (A2) the phase of the bases $\{\Theta_k(\mathbf{R},\{\mathbf{r}\})\}$ are not fixed because the eigenvalue equation is unchanged under the transformation $\tilde{\Theta}_k(\mathbf{R},\{\mathbf{r}\}) = \Theta_k(\mathbf{R},\{\mathbf{r}\})\exp[-i\theta(\mathbf{R})]$. However, the Berry connections of the transformed bases $\tilde{\mathbf{A}}_{k,q}(\mathbf{R}) \equiv i\int d\mathbf{r}\tilde{\Theta}_k^*(\mathbf{R},\{\mathbf{r}\})\nabla_{\mathrm{R}}\tilde{\Theta}_q(\mathbf{R},\{\mathbf{r}\})$ accordingly become

$$\tilde{\mathbf{A}}_{k,q}(\mathbf{R}) = \begin{cases}\mathbf{A}_{k,q}(\mathbf{R}), & k\neq q\\ \mathbf{A}_{k,k}(\mathbf{R}) + \nabla_{\mathrm{R}}\theta(\mathbf{R}), & k = q\end{cases}. \tag{A12}$$

Therefore $\mathbf{A}_{k,k}(\mathbf{R})$ depends on the choice of the phase factor $\theta(\mathbf{R})$ and thus we cannot decide its perturbation order. This is actually the $U(1)$ gauge transformation and the physical observations are not influenced by the specific choice of the phase factor. In our problem of the interface exciton, this induced gauge field can be canceled out by choosing the proper bases as $\mathbf{A}_{k,k}(\mathbf{R}) = 0$ for any k.

To apply the standard perturbation theory, we rewrite Eq. (A3) in a matrix form as

$$\Phi(\mathbf{R},\{\mathbf{r}\}) = \Psi(\mathbf{R})^T\cdot\Theta(\mathbf{R},\{\mathbf{r}\}), \tag{A13}$$

where the coefficient vector $\Psi(\mathbf{R})$ and the base vector $\Theta(\mathbf{R},\mathbf{r})$ are

$$\Psi(\mathbf{R}) = \begin{bmatrix}\Psi_1(\mathbf{R})\\ \Psi_2(\mathbf{R})\\ \vdots\end{bmatrix}, \Theta(\mathbf{R},\mathbf{r}) = \begin{bmatrix}\Theta_1(\mathbf{R},\{\mathbf{r}\})\\ \Theta_2(\mathbf{R},\{\mathbf{r}\})\\ \vdots\end{bmatrix}. \tag{A14}$$

The Eqs. (A4) are rewritten as $(H^0(\mathbf{R}) + H^1(\mathbf{R}))\Psi(\mathbf{R}) = E\Psi(\mathbf{R})$ with corresponding Hamiltonians in the matrix form as

$$H^0(\mathbf{R}) = \begin{bmatrix} H_1^0(\mathbf{R}) & 0 & \cdots \\ 0 & H_2^0(\mathbf{R}) & \cdots \\ \vdots & \vdots & \ddots \end{bmatrix} \tag{A15}$$

and

$$H^1(\mathbf{R}) = \begin{bmatrix} H_1^1(\mathbf{R}) & H_{12}^1(\mathbf{R}) & \cdots \\ H_{21}^1(\mathbf{R}) & H_2^1(\mathbf{R}) & \cdots \\ \vdots & \vdots & \ddots \end{bmatrix}. \tag{A16}$$

Here all the first order and the second order perturbations are included into $H^1(\mathbf{R})$. By applying the standard perturbation theory, the second order eigenenergy and wave function, respectively, as $E_p = E_p^0 + E_p^1$ and $\Psi_p(\mathbf{R}) = \Psi_p^0(\mathbf{R}) + \Psi_p^1(\mathbf{R})$, where

$$E_p^1 = \sum_{k \neq p} \frac{\hbar^2}{2M} \int d\mathbf{R} \Psi_p^{0,*}(\mathbf{R}) \mathbf{A}_{p,k}(\mathbf{R}) \cdot \mathbf{A}_{k,p}(\mathbf{R}) \Psi_p^0(\mathbf{R}), \tag{A17}$$

$$\Phi_p^1(\mathbf{R}) = \sum_{k \neq p} \frac{\int d\mathbf{R}' \Psi_k^{(0),*}(\mathbf{R}') H_{kp}^1(\mathbf{R}') \Psi_p^{(0)}(\mathbf{R}')}{E_p^0 - E_k^0} \Psi_k^0(\mathbf{R}), \tag{A18}$$

the zeroth order eigenenergy and wave function are determined by $H^0(\mathbf{R})$ as $H^0(\mathbf{R})\Psi_p^0(\mathbf{R}) = E_p^0 \Psi_p^0(\mathbf{R})$ and $H_{kp}^1(\mathbf{R}')$ is the element of perturbation Hamiltonian $H^1(\mathbf{R})$.

---

[1] T. Mimura, S. Hiyamizu, T. Fujii, and K. Nanbu, Jpn. J. Appl. Phys. **19**, L225 (1980).

[2] P. S. Zory, *Quantum Well Lasers* (Academic Press, New York, 1993).

[3] H. Morkoc and S. N. Mohammad, Science **267**, 51 (1995).

[4] E. Yablonovitch, T. Gmitter, R. M. Swanson, and Y. H. Kwark, Appl. Phys. Lett. **47**, 1211 (1986).

[5] G. Bastard, *Wave Mechanics Applied to Semiconductor Heterostructures* (Les Editions de Physique, Paris, 1988).

[6] D. Grundman, M. Ledentsov, and N. N. Bimberg, *Quantum Dot Heterostructures* (John Wiley Sons, Chichester, 1998).

[7] J. Li, D. Wang, and R. R. LaPierre, *Advances in III-V Semiconductor Nanowires and Nanodevices* (Bentham Science Publishers, Oak Park, IL, 2011).

[8] G.-B. Liu, D. Xiao, Y. Yao, X. Xu, and W. Yao, Chem. Soc. Rev. **44**, 2643 (2015).

[9] K. F. Mak, C. Lee, J. Hone, J. Shan, and T. F. Heinz, Phys. Rev. Lett. **105**, 136805 (2010).

[10] A. Splendiani, L. Sun, Y. Zhang, T. Li, J. Kim, C.-Y. Chim, G. Galli, and F. Wang, Nano Lett. **10**, 1271 (2010).

[11] Q. H. Wang, K. Kalantar-Zadeh, A. Kis, J. N. Coleman, and M. S. Strano, Nat. Nanotechnol. **7**, 699 (2012).

[12] X. Xu, W. Yao, D. Xiao, and T. F. Heinz, Nat. Phys. **10**, 343 (2014).

[13] T. Cao, G. Wang, W. Han, H. Ye, C. Zhu, J. Shi, Q. Niu, P. Tan, E. Wang, B. Liu, and J. Feng, Nat. Commun. **3**, 887 (2012).

[14] A. M. Jones, H. Yu, N. J. Ghimire, S. Wu, G. Aivazian, J. S. Ross, B. Zhao, J. Yan, D. G. Mandrus, D. Xiao, W. Yao, and X. Xu, Nat. Nanotechnol. **8**, 634 (2013).

[15] K. F. Mak, K. He, J. Shan, and T. F. Heinz, Nat. Nanotechnol. **7**, 494 (2012).

[16] W. Yao, D. Xiao, and Q. Niu, Phys. Rev. B **77**, 235406 (2008).

[17] R. Cheng, D. Li, H. Zhou, C. Wang, A. Yin, S. Jiang, Y. Liu, Y. Chen, Y. Huang, and X. Duan, Nano Lett. **14**, 5590 (2014).

[18] M.-H. Chiu, M.-Y. Li, W. Zhang, W. T. Hsu, W.-H. Chang, M. Tettones, H. Terrones, and L.-J. Li, ACS Nano **8**, 9649 (2014).

[19] H. Fang, C. Battaglia, C. Carraro, S. Nemsak, B. Ozdol, J. S. Kang, H. A. Bechtel, S. B. Desai, F. Kronast, A. A. Unal, G. Conti, C. Conlon, G. K. Palsson, M. C. Martin, A. M. Minor, C. S. Fadley, E. Yablonovitch, R. Maboudian, and A. Javey, Proc. Natl. Acad. Sci. USA **111**, 6198 (2014).

[20] M. M. Furchi, A. Pospischil, F. Libisch, J. Burgdörfer, and T. Mueller, Nano Lett. **14**, 4785 (2014).

[21] X. Hong, J. Kim, S. F. Shi, Y. Zhang, C. Jin, Y. Sun, S. Tongay, J. Wu, Y. Zhang, and F. Wang, Nat. Nanotechnol. **9**, 682 (2014).

[22] C.-H. Lee, G.-H. Lee, A. M. van der Zande, W. Chen, Y. Li, M. Han, X. Cui, G. Arefe, C. Nuckolls, T. F. Heinz, J. Guo, J. Hone, and P. Kim, Nat. Nanotechnol. **9**, 676 (2014).

[23] P. Rivera, J. R. Schaibley, A. M. Jones, J. S. Ross, S. Wu, G. Aivazian, P. Klement, K. Seyler, G. Clark, N. J. Chimire, J. Yan, D. G. Mandrus, W. Yao, and X. Xu, Nat. Commun. **6**, 6242 (2015).

[24] P. Rivera, K. L. Seyler, H. Yu, J. R. Schaibley, J. Yan, D. G. Mandrus, W. Yao, and X. Xu, Science **351**, 688 (2016).

[25] X. Chen, Y. Qiu, H. Yang, G. Liu, W. Zheng, W. Feng, W. Cao, W. Hu, and PingAn Hu, ACS Appl. Mater. Interfaces **9**, 1684 (2017).

[26] K. Bogaert, S. Liu, J. Chesin, D. Titow, S. Gradecak, and S. Garaj, Nano Lett. **16**, 5129 (2016).

[27] K. Chen, X. Wan, J. Wen, W. Xie, Z. Kang, X. Zeng, H. Chen, and J.-B. Xu, China ACS Nano **9**, 9868 (2015).

[28] K. Chen, X. Wan, W. Xie, J. Wen, Z. Kang, X. Zeng, H. Chen, and J. Xu, Adv. Mater. **27**, 6431 (2015).

[29] X. Duan, C. Wang, J. C. Shaw, R. Cheng, Y. Chen, H. Li, X. Wu, Y. Tang, Q. Zhang, A. Pan, J. Jiang, R. Yu, Y. Huang, and X. Duan, Nat. Nanotechnol. **9**, 1024 (2014).

[30] Y. Gong, S. Lei, G. Ye, B. Li, Y. He, K. Keyshar, X. Zhang, Q. Wang, J. Lou, Z. Liu, R. Vajtai, W. Zhou, and P. M. Ajayan, Nano Lett. **15**, 6135 (2015).

[31] Y. Gong, J. Lin, X. Wang, G. Shi, S. Lei, Z. Lin, X. Zou, G. Ye, R. Vajtai, B. I. Yakobson, H. Terrones, M. Terrones, B. K. Tay, J. Lou, S. T. Pantelides, Z. Liu, W. Zhou, and P. M. Ajayan, Nat. Mater. **13**, 1135 (2014).

[32] C. Huang, S. Wu, A. M. Sanchez, J. J. P. Peters, R. Beanland, J. S. Ross, P. Rivera, W. Yao, D. H. Cobden, and X. Xu, Nat. Mater. **13**, 1096 (2014).

[33] M.-Y. Li, Y. Shi, C.-C. Cheng, L.-S. Lu, Y.-C. Lin, H.-L. Tang, M.-L. Tsai, C.-W. Chu, K.-H. Wai, J.-H. He, W.-H. Chang, K. Suenaga, and L.-J. Li, Science **349**, 524 (2015).

[34] M. Mahjouri-Samani, M.-W. Lin, K. Wang, A. R. Lupini, J. Lee, L. Basile, A. Boulesbaa, C. M. Rouleau, A. A. Puretzky,

I. N. Ivanov, K. Xiao, M. Yoon, and D. B. Geohegan, Nat. Commun. **6**, 7749 (2015).

[35] L. H. G. Tizei, Y.-C. Lin, M. Mukai, H. Sawada, A.-Y. Lu, L.-J. Li, K. Kimoto, and K. Suenaga, Phys. Rev. Lett. **114**, 107601 (2015).

[36] X.-Q. Zhang, C.-H. Lin, Y.-W. Tseng, K.-H. Huang, and Y.-H. Lee, Nano Lett. **15**, 410 (2015).

[37] Z. Zhang, P. Chen, X. Duan, K. Zang, J. Luo, and X. Duan, Science **357**, 788 (2017).

[38] J. S. Ross, P. Klement, A. M. Jones, N. J. Ghimire, J. Yan, D. G. Mandrus, T. Taniguchi, K. Watanabe, K. Kitamura, W. Yao, D. H. Cobden, and X. Xu, Nat. Nanotechnol. **9**, 268 (2014).

[39] B. W. H. Baugher, H. O. H. Churchill, Y. Yang, and P. Jarillo-Herrero, Nat. Nanotechnol. **9**, 262 (2014).

[40] A. Pospischil, M. M. Furchi, and T. Mueller, Nat. Nanotechnol. **9**, 257 (2014).

[41] S. B. Desai, S. R. Madhvapathy, A. B. Sachid, J. P. Llinas, Q. Wang, G. H. Ahn, G. Pitner, M. J. Kim, J. Bokor, C. Hu, H.-S. Philip Wong, and A. Javey, Science **354**, 99 (2016).

[42] A. M. van der Zande, J. Kunstmann, A. Chernikov, D. A. Chenet, Yu Meng You, XiaoXiao Zhang, P. Y. Huang, T. C. Berkelbach, L. Wang, F. Zhang, M. S. Hybertsen, D. A. Muller, D. R. Reichman, T. F. Heinz, and J. C. Hone, Nano. Lett. **14**, 3869 (2014).

[43] H. Yu, Y. Wang, Q. Tong, X. Xu, and W. Yao, Phys. Rev. Lett. **115**, 187002 (2015).

[44] H. Yu, G.-B. Liu, J. Tang, X. Xu, and W. Yao, Sci. Adv. **3**, e1701696 (2017).

[45] F. Wu, T. Lovorn, and A. H. MacDonald, Phys. Rev. B **97**, 035306 (2018).

[46] H. Yu, G.-B. Liu, and W. Yao, 2D Materials **5**, 035021 (2018).

[47] A. M. Jones, H. Yu, J. S. Ross, P. Klement, N. J. Ghimire, J. Yan, D. G. Mandrus, W. Yao, and X. Xu, Nat. Phys. **10**, 130 (2014).

[48] J. P. Eisenstein and A. H. MacDonald, Nature (London) **432**, 691 (2004).

[49] A. A. High, E. E. Novitskaya, L. V. Butov, M. Hanson, and A. C. Gossard, Science **321**, 229 (2008).

[50] L. V. Keldysh, JETP Lett. **29**, 658 (1978).

[51] P. Cudazzo, I. V. Tokatly, and A. Rubio, Phys. Rev. B **84**, 085406 (2011).

[52] T. C. Berkelbach, M. S. Hybertsen, and D. R. Reichman, Phys. Rev. B **88**, 045318 (2013).

[53] A. Chernikov, T. C. Berkelbach, H. M. Hill, A. Rigosi, Y. Li, O. B. Aslan, D. R. Reichman, M. S. Hybertsen, and T. F. Heinz, Phys. Rev. Lett. **113**, 076802 (2014).

[54] K. He, N. Kumar, L. Zhao, Z. Wang, K. F. Mak, H. Zhao, and J. Shan, Phys. Rev. Lett. **113**, 026803 (2014).

[55] D. Y. Qiu, F. H. da Jornada, and S. G. Louie, Phys. Rev. Lett. **111**, 216805 (2013).

[56] H. Yu, G.-B. Liu, P. Gong, X. Xu, and W. Yao, Nat. Commun. **5**, 3876 (2014).

[57] D. S. Citrin, Phys. Rev. B **47**, 3832 (1993).

[58] B. K. Kendricka, C. A. Meadb, and D. G. Truhlarc, Chem. Phys. **277**, 31 (2002).

[59] C.-P. Sun and M.-L. Ge, Phys. Rev. D **41**, 1349 (1990).

[60] D. Xiao, G.-B. Liu, W. Feng, X. Xu, and W. Yao, Phys. Rev. Lett. **108**, 196802 (2012).

[61] G.-B. Liu, W.-Y. Shan, Y. Yao, W. Yao, and D. Xiao, Phys. Rev. B **88**, 085433 (2013).

[62] J. M. Rorison, Phys. Rev. B **48**, 4643 (1993).

[63] J. Warnock, B. T. Jonker, A. Petrou, W. C. Chou, and X. Liu, Phys. Rev. B **48**, 17321 (1993).

[64] M. H. Degani and G. A. Farias, Phys. Rev. B **42**, 11701 (1990).

[65] X. L. Yang, S. H. Guo, F. T. Chan, K. W. Wong, and W. Y. Ching, Phys. Rev. A **43**, 1186 (1991).

[66] R.-B. Liu, W. Yao, and L. J. Sham, Adv. Phys. **59**, 703 (2010).